*energies*

MDPI

*Article*

# Start-Up and Fault-Ride-Through Strategy for Offshore Wind Power via DRU-HVDC Transmission System

**Yiting Zhang [1], Wenjiang Zhu [2], Cheng Tang [2], Ni Liu [1], Sinan Li [1] and Hong Wang [1,*]**

[1] School of Mechanical Engineering and Automation, Harbin Institute of Technology, Shenzhen 518055, China; 22s153253@stu.hit.edu.cn (Y.Z.); 20b353009@stu.hit.edu.cn (N.L.); lisinan@stu.hit.edu.cn (S.L.)
[2] China Nuclear Power Technology Research Institute Co., Ltd., Shenzhen 518031, China; zhuwenjiang@cgnpc.com.cn (W.Z.); tangcheng@cgnpc.com.cn (C.T.)
* Correspondence: hongwang@hit.edu.cn

**Abstract:** The diode-rectifier unit (DRU)-based high-voltage direct current (HVDC) transmission system offers an economical solution for offshore wind power transmission. However, this approach requires offshore wind farms to establish a strong grid voltage. To meet this requirement while fulfilling the dynamic characteristics of the DRU, this paper proposes an advanced grid-forming (GFM) control strategy for offshore wind turbines connected to DRU-HVDC. The strategy incorporates a P-U controller and a Q-$\omega$ controller based on reactive power synchronization. Furthermore, a novel virtual power-based pre-synchronization method and an adaptive virtual impedance technique are integrated into the proposed GFM control to improve system performance during wind turbine (WT) integration and low-voltage ride-through (LVRT) scenarios. The virtual power-based pre-synchronization method reduces voltage spikes during the integration of new wind turbines, while the adaptive virtual impedance technique effectively suppresses fault currents during low-voltage faults, enabling faster recovery. Simulation results validate the effectiveness of the proposed GFM control strategy, demonstrating improved start-up and LVRT performance through the pre-synchronization and adaptive virtual impedance methods.

**Keywords:** DRU-HVDC; grid-forming; virtual impedance; current limiting; pre-synchronization; wind farm

check for updates

**Citation:** Zhang, Y.; Zhu, W.; Tang, C.; Liu, N.; Li, S.; Wang, H. Start-Up and Fault-Ride-Through Strategy for Offshore Wind Power via DRU-HVDC Transmission System. *Energies* **2024**, *17*, 4968. https://doi.org/10.3390/en17194968

Academic Editor: Oscar Barambones

Received: 5 August 2024
Revised: 29 September 2024
Accepted: 30 September 2024
Published: 4 October 2024

**Copyright:** © 2024 by the authors. Licensee MDPI, Basel, Switzerland. This article is an open access article distributed under the terms and conditions of the Creative Commons Attribution (CC BY) license (https://creativecommons.org/licenses/by/4.0/).

## 1. Introduction

Offshore wind farms are the mainstream of future wind power generation for their consistent wind energy and abundant space [1,2]. With the rapid expansion of offshore wind power exploitation, there is an urgent need for reliable and efficient wind power transmission technologies. At present, offshore wind power transmission systems can be classified into two categories: high-voltage-alternating-current (HVAC) and high-voltage-direct-current (HVDC). In offshore wind power generation systems, the distance between the offshore wind farm and the onshore converter can reach up to 100 km. This is a limitation for the HVAC transmission system due to the associated cost and capacitance effect of AC cable [3]. HVDC is considered to be the preferred solution for offshore wind power transmission system as it is independent of cable capacitance in scenarios exceeding 100 km in length and offers a low cost of ownership.

To date, several HVDC wind transmission systems have been proposed in different studies. Line-commuted-converter (LCC)-based HVDC offers advantages such as high voltage, high capacity, and low cost. However, they are limited by their requirement to be connected to strong grids and their significant consumption of reactive power, which can lead to commutation failures. In contrast, voltage-source-converter (VSC)-based HVDC can operate in any type of grid, allowing for decoupled control of active and reactive power. However, they are typically more expensive than LCC-HVDC and cannot effectively manage DC short circuit faults [4]. Modular-multilevel-converter (MMC) based HVDCs possess

the capability for fault current blocking and high efficiency; however, they are associated with a large footprint, significant investment costs, and complex control strategies [5]. Diode-rectifier-unit (DRU)-based HVDC systems offer lower costs, reduced complexity, smaller loss, high reliability and compatibility with various grid types, making them an ideal solution for HVDC transmission systems in offshore wind farms.

However, the commutation voltage of the DRU-HVDC system must be supplied by the grid-side converter (GSC) of the wind turbine (WT), which implies that conventional grid-following (GFL) cannot be utilized in GSC due to the absence of voltage support. Thus, the GSCs of WTs, which are shown in Figure 1, are mostly controlled in grid-forming (GFM) mode in the DRU-HVDC transmission system. In the figure, PCC is the point of common coupling; B1 represents the part before the HVDC transmission; B2 represents the part after the HVDC transmission; ac represents alternating current and dc represents direct current.

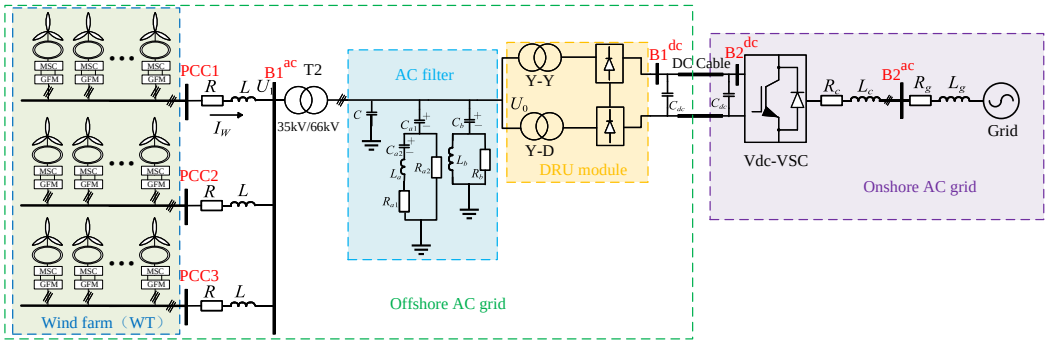


**Figure 1.** Schematic Diagram of Offshore Wind Farm Connected to DRU-HVDC System.

To enhance the performance of GFM-based GSCs, it is essential to clarify the control strategy, start-up and fault-ride-through (FRT) strategies of GFM-based GSCs in DRU-HVDC systems.

The GFM control strategies of GSCs can be classified into two categories: centralized control and decentralized control. A central control unit coordinates the operation of all GSCs [6] , with communication bandwidth being a critical factor. To reduce communication burdens, a strategy employing active power-voltage (P-U) and reactive power-frequency (Q-$\omega$) droop is proposed in [7]; however, propagation delay remains a concern. In contrast, decentralized control can establish voltage and frequency at the point of common coupling (PCC) with lower communication bandwidth. Several synchronization methods have been proposed by researchers within this framework, which can be categorized into two groups: (1) phase reference is given directly, such as phase-locked loop (PLL) and Global positioning system (GPS); (2) phase reference is given indirectly, such as power synchronization.

In the direct phase reference method, GPS is utilized to provide phase references, as mentioned in [8]. However, GPS devices can be costly, and phase reference values may vary due to differences in startup times. To address this problem, distributed PLL is proposed in [9], where GSCs obtain phase reference locally through PLL. However, the utilization of PLL can introduce stability risks [10]. In contrast, the indirect phase reference method has made notable progress in reactive power synchronization. In [11], a reactive power-frequency droop controller has been proposed to generate synchronous phase angles between units; however, it may not be applicable in weak wind conditions. To address this issue, a reactive power synchronization method with AC voltage compensation is proposed in [10].

The start-up process for GSCs in DRU-HVDC can be divided into black start-up and new WT integration. During the black start-up procession, offshore wind farms (OWFs) are unable to draw power due to the unidirectional characteristic of DRU. Several energy solutions for black start-ups have been proposed. A hybrid topology is used in [12,13], comprising of DRU and an auxiliary MMC for start-up. In [14], an external DC source is incorporated into the DC bus of the back-to-back converter, allowing for the integration of energy storage as discussed in [15]. WTs can achieve self-start-up ability when equipped

with energy storage. To simplify the start-up process, external batteries are used to start up WTs in this study, without delving into the specifics of the black startup procedure.

During new WTs integration, the GSCs may become unsynchronized with the offshore grid due to the slow response of power synchronization, leading to large voltage and current spikes. To address this issue, several approaches have been proposed. Ref. [16] employs PLL to obtain phase for pre-synchronization. However, this method may exhibit poor performance under weak grid conditions, and the improper integration of PLL can lead to system instability. Recently, a decentralized method named virtual oscillator control (VOC) has been carried out in [17,18]. The initial phase can be obtained easily and responds quickly with this method. However, certain conditions are required to achieve a reliable phase reference in VOC, which may not be applicable in weak offshore AC grid conditions. Ref. [19] employs the virtual power method, which avoids the use of PLL and demonstrates effective performance in weak grid conditions.

FRT capability is crucial for compliance with grid code requirements. However, the existing studies on DRU-HVDC systems pay little attention to FRT. Most research primarily focuses on faults in onshore AC grids. These studies address suppressing active power during onshore AC grid faults and limit over-voltage in HVDC bus [20]. Little attention has been given to LVRT control strategies in offshore AC systems for DRU-HVDC systems. Current research on LVRT strategies can be categorized into GFL-based and GFM-based strategies. GFL-based strategies inject reactive power into the grid using techniques such as FCS-MPC [21], sliding mode control [22], and additional energy storage systems [23]. Although these methods can be effective in traditional LVRT scenes, they are unable to handle offshore AC voltage after recovery in DRU-HVDC. Additionally, the mode transition process between GFL and GFM is rather slow and may lead to over-current issues [24]. GFM strategies mainly concentrate on adopting strategies such as droop control and modifications on virtual synchronous generators(VSG) [25]. Current limitation control is applied to VSG control in some approaches [26,27]. However, poor current limiting ability and system stability may occur during asymmetric faults. Virtual impedance is adopted in [28] , but constant impedance leads to limited power recovery response. Key aspects, such as fast response and self-recovery LVRT strategies still require further attention.

The main contributions of this paper can be summarized as threefold:

- A power synchronized GFM control strategy and analysis of offshore wind farms based on DRU-HVDC and control strategy is proposed in this study. The dynamic stability of self-synchronous response under power disturbances is analyzed. The proposed GFM control strategy demonstrates favorable plug-and-play characteristics in the DRU-HVDC system.
- A comprehensive analysis of multiple GSC start-up processes is proposed in this study. Pre-synchronization for the parallel operation of multiple GSCs has not been implemented in DRU-HVDC systems for offshore wind power generation before. An improved virtual power-based pre-synchronization method is proposed to optimize the smooth integration of several GSCs. The mechanism of the novel pre-synchronization method is analyzed in detail.
- An adaptive virtual impedance-based LVRT strategy is first introduced for GSCs connected to DRU-HVDC systems. The proposed method adjusts the virtual impedance adaptively to effectively suppress fault current and facilitates rapid recovery after fault clearance. Additionally, a complete adaptive virtual impedance calculation process is provided. Compared to conventional current-limiting and fixed virtual impedance-based LVRT strategy, the proposed method offers a faster current-limiting response and rapid recovery performance in the DRU-HVDC system.

This paper is organized as follows: Section 2 provides an overview of the DRU-HVDC system structure and analyzes the model of the DRU-HVDC system. Building on this model, the fundamental concepts of the GFM control strategy and power synchronization methods for GSCs are introduced. Additionally, this section presents the proposed start-up and LVRT strategies, including a comprehensive analysis of the virtual power-based pre-

synchronization method and the adaptive virtual impedance strategy. Section 3 presents simulation results to verify the effectiveness of the proposed control strategy. Section 4 provides a discussion and comparison of the proposed strategy with existing research. Finally, Section 5 summarizes the key findings of the paper.

## 2. Advanced Control Methodology for Offshore Wind Turbines Connected to DRU-HVDC

### *2.1. System Topology*

#### 2.1.1. Topology of Proposed DRU-HVDC System

Figure 1 illustrates the system topology of the DRU-HVDC-based offshore wind power transmission system. This system consists of wind turbines (WTs) equipped with back-to-back converters connected to an offshore AC grid, an offshore rectifier station with filter banks, and an onshore converter station linked to the onshore grid. Multiple WTs are connected to the PCC through back-to-back converters, each comprising a Machine Side Converter (MSC) and a GSC. Wind power is transmitted via submarine cables and collected at the AC bus (shown in Figure 1 $B1^{ac}$ ). Subsequently, the AC voltage is stepped up by transformer T2, enabling power transmission through the DRU-HVDC system.

Due to the uncontrollable characteristics of diodes in offshore converters, the voltage of the offshore AC grid is regulated by the GSCs, while the DC voltage of back-to-back converters is controlled by MSCs. To reduce total harmonic distortion(THD), the DRU utilizes a 12-pulse rectifier topology consisting of a Y-Y connected transformer and a Y-D connected transformer in series, along with a filter bank to compensate for reactive power and eliminate higher-order harmonics. The onshore station employs grid-following control to regulate the DC voltage of the DRU-HVDC link.

#### 2.1.2. Equivalent Model of DRU

DRU is equivalent to a thyristor rectifier with zero firing angle. Thus, the DRU output voltage can be determined from the line impedance and the DRU characteristics [29], and is given by

$$U_{dru} = 2\left(\frac{3\sqrt{2}U_0}{\pi T_{dr}} - 3X_T\frac{I_{dc}}{\pi}\right) \tag{1}$$

where $U_0$ is the root-mean-square(RMS) voltage value of the offshore AC power grid, $I_{dc}$ and $U_{dru}$ are the DC current and DC voltage of the DRU station, and $T_{dr}$, $L_T$ and $X_T$ are the transformer ratio, leakage inductor value and leakage inductance, respectively.

The DC-side current and active power of DRU can be calculated as

$$I_{dc} = \frac{\sqrt{2}U_0}{T_{dr}X_T} - \frac{\pi U_{dru}}{6X_T} \tag{2}$$

$$P_{dru} = U_{dru} \times I_{dc} = \frac{\sqrt{2}U_0U_{dru}}{T_{dr}} - \frac{\pi U_{dru}^2}{6X_T} \tag{3}$$

where $P_{dru}$ is the active power transmitted by the DRU station.

Assuming that the system operates at 100% efficiency, the turbine output power and the DRU transmitted power are equal. Thus, the active and reactive power generated by the wind farm can be expressed as

$$P_{WT} = P_{dru} = \frac{\sqrt{2}U_0U_{dru}}{T_{dr}} - \frac{\pi U_{dru}^2}{6X_T} \tag{4}$$

Assuming that the DRU station operates at the power factor angle $\varphi$, the reactive power $Q_{dru}$ can be given as

$$Q_{dru} = P_{dru} \tan \varphi = P_{dru} \sqrt{\frac{1}{\cos^2 \varphi} - 1} = P_{dru} \sqrt{\frac{1}{(U_d/U_0)^2} - 1} \tag{5}$$

where $Q_{dru}$ is the reactive power consumed by the DRU station.

The sum of the reactive power emitted by the wind farm and the reactive power produced by the filter ($Q_{fil} = wCU_0^2$) equals the reactive power transmitted through the DRU system and is given by

$$Q_{WT} = Q_{dru} - Q_{fil} = P_{dru} \sqrt{\frac{1}{(U_{dru}/U_0)^2} - 1} - \omega C U_0^2 \tag{6}$$

2.1.3. Sensitivity Model of DRU

One can get four types of sensitivity from Equations (4) and (6), and is given by the following:

$$\begin{cases} \frac{\partial P_{\mathrm{WT}}}{\partial U_{\mathrm{WT}}} = \frac{C_1}{f} \\ \frac{\partial P_{\mathrm{WT}}}{\partial f} = -C_1 \frac{U_0}{f^2} + \frac{C_2}{f^2} = -\frac{P_{\mathrm{dru}}}{f} \\ \frac{\partial Q_{\mathrm{WT}}}{\partial U_{\mathrm{wt}}} = \frac{C_3 U_0 (C_1 U_0 - C_2)}{f\sqrt{C_3 U_0^2 - 1}} + \frac{C_1}{f}\sqrt{C_3 U_0^2 - 1} - 4\pi f C_0 U_0 \\ \frac{\partial Q_{\mathrm{WT}}}{\partial f} = \left(-C_1 \frac{U_0}{f^2} + \frac{C_2}{f^2}\right)\sqrt{C_3 U_0^2 - 1} - 2\pi C_0 U_0^2 = -\frac{Q_{\mathrm{dru}} + Q_{\mathrm{fil}}}{f} \end{cases} \tag{7}$$

where $C_1 = \frac{\sqrt{2}U_{dru}}{2\pi T_{dr} L_T}$, $C_2 = \frac{U_{dru}^2}{12 L_T}$, $C_3 = \frac{18}{\pi^2 T_{dr}^2 U_{dru}^2}$, respectively.

It can be seen from Equation (7) that the partial derivative of voltage with respect to the output active power of the DRU is positive and independent of the output active power. The partial derivative of the output reactive power of the DRU with respect to frequency is negative and is related to reactive power, remaining unaffected by the system's output active power. Furthermore, the other two sensitivity models are influenced by both frequency and voltage, which may limit their applicability in droop control.

Based on the analysis of Equation (7), a clear sensitivity characteristic with "reactive power-frequency and active power-voltage droop" of DRU can be obtained, which is essential for the GFM control strategy of GSC converters connected to DRU-HVDC.

*2.2. Control Strategy of GSC Converter*

Figure 2 shows the GFM control block of the DRU-HVDC transmission system for offshore wind power, including the outer power control loop, along with the voltage and current loop.

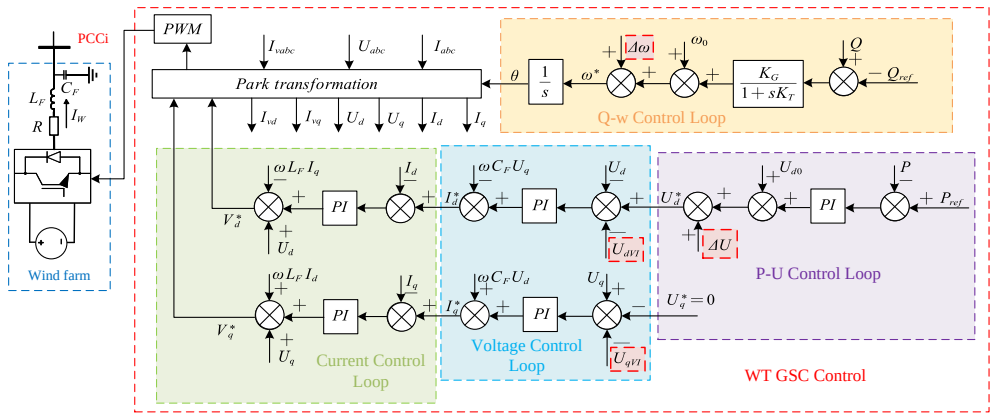


**Figure 2.** Control block diagram of the GSC of the WT.

2.2.1. Power Control Loop

In the DRU-HVDC system, the GSCs regulate the voltage and frequency of the offshore AC grid by adjusting active and reactive power [30]. Based on Equation (7), active power can be utilized to control the voltage amplitude of the offshore AC grid, demonstrating a positive relationship between voltage and active power. The P-U controller of GSC is depicted in purple in Figure 2, and the AC voltage references in $dq$-axis coordinate system are

$$\begin{cases} U_d^* = U_{ref} = U_0 + \left(K_P + \frac{K_I}{s}\right)\left(P_{ref} - P\right) \\ U_q^* = 0 \end{cases} \tag{8}$$

where $U_d^*$ and $U_q^*$ are the $d$-axis and $q$-axis component reference values of the PCC voltage, $K_I$ and $K_P$ are the proportional parameter and the integral parameter of the controller, respectively.

Similarly, reactive power can be used to control the frequency of offshore AC grid based on Equation (7). Therefore, a reactive power-frequency controller for GSC is applied. The Q-$\omega$ control can be expressed as

$$\omega = \omega_0 + \frac{K_G}{1 + sK_T}\left(Q - Q_{ref}\right) \tag{9}$$

where $\omega_0$ is the frequency reference value, $Q$ and $Q_{ref}$ are the actual and reference reactive power of WT, $K_G$ and $K_T$ are the control parameters of the first-order inertial element in the controller.

Each WT can ultimately achieve uniform reactive power sharing by establishing the same reference. The framework of the reactive power-frequency control is illustrated in the yellow block in Figure 2. Additionally, by integrating the frequency reference value of the AC system, the angle for coordinate transformation is given by

$$\theta = \frac{\omega_0}{s}\omega \tag{10}$$

2.2.2. Voltage and Current Control Loop

Similar to the typical GFM control, the inner control loop of WT consists of a voltage controller and a current controller. The structure is shown in the green and blue sections of Figure 2. The current inner loop facilitates rapid response and current limiting during AC faults, while the voltage inner loop enables the WTs to function as voltage sources. The inner voltage controller is given by

$$\begin{cases} C_F \frac{dU_{1d}}{dt} = I_{Wd} - I_{Cd} + \omega C_F U_{1q} \\ C_F \frac{dU_{1q}}{dt} = I_{Wq} - I_{Cq} + \omega C_F U_{1d} \end{cases} \tag{11}$$

and the inner current controller is given by

$$\begin{cases} RI_{Wd} + L_F \frac{dI_{Wd}}{dt} = U_{Cd} - U_{1d} + \omega L_F I_{Wq} \\ RI_{Wq} + L_F \frac{dI_{Wq}}{dt} = U_{Cq} - U_{1q} + \omega L_F I_{Wd} \end{cases} \tag{12}$$

where $C_F$ and $L_F$ are the filter capacitor and inductance of GSC, $U_{1d}$ and $U_{1q}$ are the final output voltage of WT, $I_{Wd}$ and $I_{Wq}$ are the final output current of WT, $I_{Cd}$ and $I_{Cq}$ are the current flowing into the filter capacitor.

2.2.3. Self-Synchronous Mechanism

The GSCs should be able to maintain stable synchronous operation under power disturbance, necessitating an analysis of synchronization stability. Phase variation, derived from power, provides insight into the synchronization stability of the system.

The power of the offshore AC system can be expressed in terms of voltage and current as

$$\begin{cases} P_1 = \frac{3}{2}(U_{1d}I_{1d} + U_{1q}I_{1q}) \\ Q_1 = \frac{3}{2}(U_{1q}I_{1d} - U_{1d}I_{1q}) \end{cases} \tag{13}$$

where $P_1$ and $Q_1$ are the active power and reactive power in the system.

Additionally, when the GSC is synchronized with the grid, $U_q = 0$ is brought into Equation (13), which can be expressed as

$$\begin{cases} P_1 = 1.5U_{1d}I_{1d} \\ Q_1 = -1.5U_{1d}I_{1q} \end{cases} \tag{14}$$

A reduction in the reactive power reference will lead to a decrease in voltage within the offshore system. Consequently, this reduction in AC voltage will result in a decrease in reactive power. The operation of the Q-$\omega$ controller will further contribute to a decline in AC frequency. Meanwhile, the reduction in reactive power from the GSCs will also lead to a decrease in the total reactive power consumed at the DRU station. In the proposed power synchronization method, GSCs redistribute reactive power according to their power capacity. As a result, the reactive power from other GSCs will also decrease, leading to a decline in frequency as managed by the Q-$\omega$ controller. Besides, the active and reactive power can be described as

$$\begin{cases} P = \frac{U_g U_1 \sin\theta}{X} \\ Q = \frac{(U_1 - U_g\cos\theta)U_1}{X} \end{cases} \tag{15}$$

Thus, the decrease in frequency will also lead to a reduction in the phase angle obtained by the integrator, consequently lowering the actual active power of the GSCs as in Equation (15). This mechanism enables the tracking of the actual active power value with the reference. The synchronization process of WTs under power disturbances is illustrated in Figure 3. This power synchronization mechanism facilitates plug-and-play capability and robustness, effectively meeting the requirements for GSCs in the DRU-HVDC system.

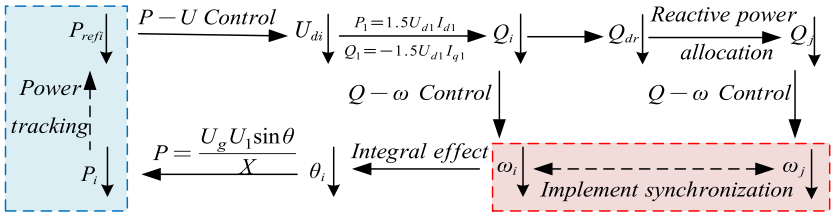


**Figure 3.** Synchronous response to power disturbances.

Overall, the proposed control strategy can support the voltage of the offshore AC grid and maintain system stability. However, under GFM control, GSCs behave as voltage sources, which limits their operation during fault and start-up conditions. Therefore, this paper proposes novel start-up and LVRT methods for GFM-based GSCs in the DRU-HVDC system.

### *2.3. Proposed Start-Up Method*

In the proposed DRU-HVDC system, GSCs are started one by one. However, it is notable that the start-up processes for the first GSC and other GSCs are different.

#### 2.3.1. Start-Up Strategy for GSCs

Offshore wind farms require additional black start-up sources to get started. There are several kinds of black start sources, such as energy storage and additional converters [12]. Numerous studies have addressed this topic, but the black start process is not considered in this study to simplify the analysis.

When the wind farm gets started, the first GSC maintains the voltage of the PCC. During this initial phase, power synchronization is not yet established. The proposed start-up strategy is outlined as follows:

The first GSC starts with constant frequency (CF) control, gradually increasing the voltage while the AC breaker closes to pre-charge the capacitor of the HVDC bus via the DRU. Once the AC voltage reaches its nominal value, the first GSC transitions to constant voltage and constant frequency (CVCF) control. Finally, upon completion of the start-up process, the first GSC adopts the Grid-Forming (GFM) control strategy.

The start-up process of other GSCs closely resembles that of the first GSC, initially operating under CF control and subsequently transitioning to CVCF control. However, there are some notable differences. Firstly, there is no requirement for the GSCs to maintain the voltage at the PCC during the start-up process; therefore, the AC breakers remain open initially. Secondly, the GSCs transition from CVCF control to GFM control upon the closure of the AC breakers at the end of the start-up process.

To facilitate a smooth transition between CVCF and GFM control strategy for GSCs, a pre-synchronization approach is employed. And this study introduces a novel virtual power based pre-synchronization method.

#### 2.3.2. Pre-Synchronization Based on Virtual Power Method

The proposed method introduces a virtual impedance between the converter and the grid, which is active only prior to grid connection. By adjusting the virtual power value of the impedance to zero, pre-synchronization of the voltage amplitude and phase is accomplished. The simplified circuit model is shown in Figure 4.

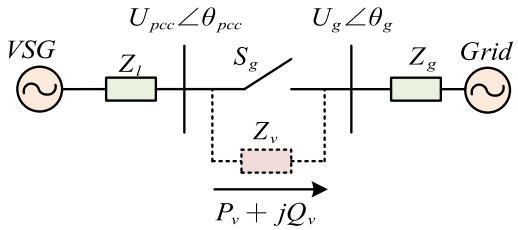


**Figure 4.** Simplified circuit for pre-synchronization.

Figure 4 shows the simplified circuit for virtual power based pre-synchronous method. Based on Ohm's law, the virtual active power and reactive power transmitted through this impedance are given by

$$\begin{cases} P_v = \frac{1}{Z_v}\left\{\left[U_{pcc}\cos(\theta_{pcc}-\theta_g) - U_g^2\right]\cos\alpha_v + U_{pcc}U_g\sin(\theta_{pcc}-\theta_g)\sin\alpha_v\right\} \\ Q_v = \frac{1}{Z_v}\left\{\left[U_{pcc}\cos(\theta_{pcc}-\theta_g) - U_g^2\right]\sin\alpha_v - U_{pcc}U_g\sin(\theta_{pcc}-\theta_g)\cos\alpha_v\right\} \\ Z_v = \sqrt{(\omega L_v)^2 + R_v^2} \\ \alpha_v = \arctan\left(\frac{\omega L_v}{R_v}\right) \end{cases} \tag{16}$$

where $U_{pcc}$ and $\theta_{pcc}$ are the voltage amplitude and phase at PCC, and $U_g$ and $\theta_g$ are the voltage amplitude and phase of the offshore AC grid. $\alpha_v$ represents the virtual impedance angle, $R_v$ represents the virtual resistance, and $L_v$ represents the virtual inductance.

Equation (16) shows that when the phase difference between virtual active power and the voltage reaches zero, the synchronization is achieved. Taking $\pi/2$ into $\alpha_v$, Equation (16) is simplified to

$$\begin{cases} P_v = \frac{U_{pcc}U_g}{Z_v}\sin(\theta_{pcc}-\theta_g) \\ Q_v = \frac{U_{pcc}}{Z_v}\left[U_{pcc} - U_g\cos(\theta_{pcc}-\theta_g)\right] \end{cases} \tag{17}$$

From Equation (17), we can conclude that the conditions $\theta_{pcc} = \theta_g$ and $U_{pcc} = U_g$ are satisfied only when the virtual active power and reactive power are both zero. Thus, it is

essential to design a control loop to ensure that both the virtual active power and reactive power are zero. This allows for successful pre-synchronization, enabling new GSCs to integrate smoothly into the grid.

To achieve virtual power synchronization, frequency and voltage magnitude compensation are incorporated into the original control strategy. The pre-synchronization compensation is illustrated in Figure 5, where the compensation values are integrated into the frequency and voltage controllers of the original control strategy. The compensated reference of frequency and voltage controllers can be expressed as

$$\begin{cases} \omega_{ref} = \omega^* + \Delta\omega \\ U_{ref} = U^* + \Delta U \end{cases} \tag{18}$$

where $\omega_{ref}$ and $U_{ref}$ are the actual reference value in the controller of GSC, $\omega^*$ and $U^*$ are the original reference value, and $\Delta\omega$ and $\Delta U$ are the compensation value.

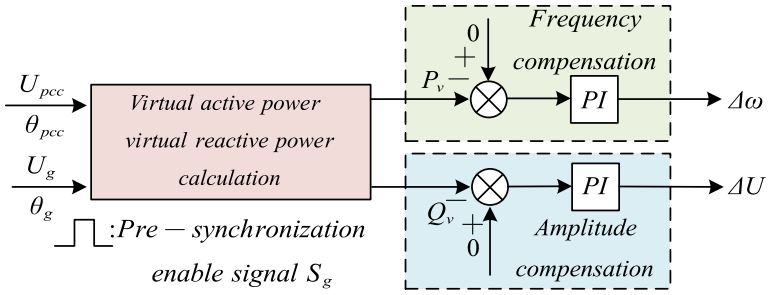


**Figure 5.** Calculation of pre-synchronization compensation.

### *2.4. Proposed LVRT Control Methods*

Without any fault current limiting measures, the fault current can exceed the normal operating range during low-voltage grid faults. The safety and reliable operation of GSCs are jeopardized. Conventional current limiting control may saturate and fail, potentially leading to system instability in GFM converters. Furthermore, setting the current limiter threshold too low may affect the system's dynamic response.

To address these issues, this study proposes a new adaptive virtual impedance (AVI) based LVRT control strategy.

#### 2.4.1. Adaptive Virtual Impedance Strategy

If the dynamic process of the transient current is ignored, the fault current can be expressed as [31]

$$\Delta I_g = \frac{\Delta U_1}{R_{eq} + jX_{eq}} \tag{19}$$

where $\Delta U_1$ is the voltage variation of the fault point, $\Delta I_g$ is the fault current caused by voltage drop, and $R_{eq}$ and $L_{eq}$ are the equivalent resistance and reactance from the grid converter to the fault point.

From Equation (19), it is evident that the fault current is proportional to the change in fault voltage and has a negative correlation with the equivalent impedance between GSCs and the fault point. By regulating the equivalent impedance, the fault current can be effectively suppressed. In other words, by implementing the virtual impedance method, the fault current can be reduced. The implementation of virtual impedance is illustrated in Figure 6.

The virtual impedance effectively limits the fault current of the converter while simultaneously reducing the reference voltage of the GSC controller. This reduction in voltage leads to a lower current reference value. Thus, the current limiting feature of the GSCs is achieved. However, fixed virtual impedance(FVI) cannot adaptively compensate based on the degree of AC voltage drop, which can result in a substantial fault current during instances of extremely low voltage.

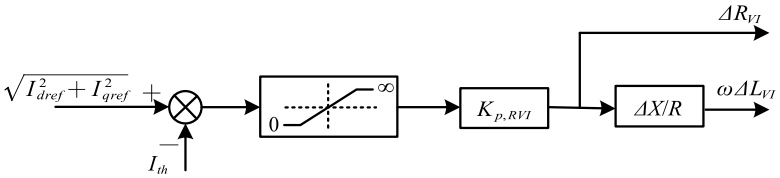


**Figure 6.** Virtual impedance calculation.

In order to suppress the overcurrent faster and ensure the dynamic performance of the system, an adaptive virtual impedance method is first used in the LVRT strategy of an offshore AC grid based on DRU-HVDC. The values of virtual resistance and reactance are adaptively adjusted based on the magnitude of the fault current. A comprehensive analysis and calculation of the adaptive virtual impedance is provided.

2.4.2. Adaptive Virtual Impedance Design

When the fault current does not exceed the threshold current, both virtual resistance and reactance are set to zero. The expressions for virtual inductance and virtual resistance are

$$\begin{cases} \Delta R_{\mathrm{VI}} = \max\left(K_{p,RVI}\left(\sqrt{I_{d,\mathrm{ref}}^2 + I_{q,\mathrm{ref}}^2} - I_{\mathrm{th}}\right), 0\right) \\ \Delta L_{\mathrm{VI}} = \Delta R_{\mathrm{VI}}(\Delta X/R) \end{cases} \tag{20}$$

where $K_{p,RVI}$ represents the gain of the current-limiting virtual impedance, $I_{th}$ is the current limiting threshold, and $\Delta X/R$ denotes the reactance-to-resistance ratio of the current-limiting virtual impedance method, which can effectively confine the fault current to an appropriate level.

The above analysis clearly indicates that designing an appropriate virtual impedance gain and $X/R$ ratio is crucial. The virtual impedance $X/R$ ratio is determined through small-signal analysis [32]. For symmetrical three-phase faults in the system, the drop in virtual impedance should be equivalent to the voltage amplitude command, as given by

$$V_{\mathrm{o}} = I_{\max} Z_{\mathrm{VI}} = I_{\max}\sqrt{R_{\mathrm{VI}}^2 + (\omega L_{\mathrm{VI}})^2} \tag{21}$$

where $I_{\max}$ is the required maximum current.

By combining Equations (20) and (21), the virtual impedance gain can be obtained as

$$\begin{cases} K_{p,RVI} = \frac{-b+\sqrt{b^2-4ac}}{2a} \\ a = (I_{\max} - I_{\mathrm{th}})^2(1+\Delta X/R)^2 \\ b = 2(I_{\max} - I_{\mathrm{th}})\left(R_{\mathrm{VI}}^0 + (\Delta X/R)\omega_0 L_{\mathrm{VI}}^0\right) \\ c = \left(R_{\mathrm{VI}}^0\right)^2 + \left(\omega_0 L_{\mathrm{VI}}^0\right)^2 - V_{\mathrm{o}}^2/I_{\max}^2 \end{cases} \tag{22}$$

Hence, the voltage drop induced by the virtual impedance is given by

$$\begin{cases} U_{d\mathrm{VI}} = \Delta R_{\mathrm{VI}} i_d - w\Delta L_{\mathrm{VI}} i_q \\ U_{q\mathrm{VI}} = \Delta R_{\mathrm{VI}} i_q + w\Delta L_{\mathrm{VI}} i_d \end{cases} \tag{23}$$

where $i_d$,$i_q$ and are the d-axis and q-axis components of the converter output current, respectively, $\omega$ is the cutoff frequency of the high-pass filter, and $\Delta R_{VI}$, $\Delta L_{VI}$ are the adaptively calculated virtual resistance and virtual inductance based on the fault current conditions.

The adaptive virtual impedance in the voltage control loop incorporating the voltage drop is illustrated in the red part within the voltage controller of Figure 2. A power-angle model can be derived for transient stability analysis, as shown in Figure 7.

Here, the active power is calculated by

$$P = \frac{3EV\sin\delta}{2Z} \tag{24}$$

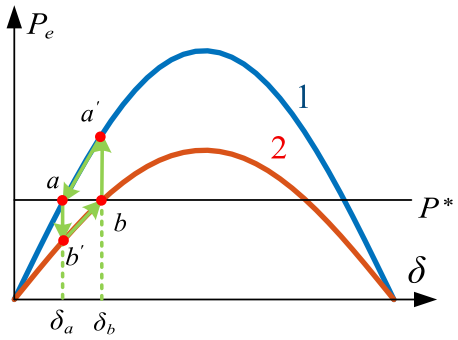


**Figure 7.** Transient stability analysis.

The power-angle relationship is shown in Figure 7. When the system operates normally, the characteristic is represented as curve 1. In contrast, the characteristic during a low voltage fault is depicted by curve 2. The overall power relationship is illustrated as follows. Initially, the GSCs work at point $a$. Following the occurrence of a low voltage fault, the power angle remains unchanged, causing the GSCs to operate at point $b^{'}$. According to Equation (24), the operating point will gradually shift to $b$ due to the condition $P^* > P_e$. A new stable operating point is established when $P^* = P_e$, facilitating normal operation during fault conditions. After the fault clearance, the operating point immediately changes to point $a$ due to the unchanged power angle. Subsequently, since $P^* < P_e$, the operating point moves to point $a$ finally, returning to the initial stable operation.

## 3. Simulation Results

As depicted in Figures 1 and 2, a case study has been conducted to validate the proposed control strategy. The system parameters are detailed in Table 1. The system consists of three wind farms, while the DC bus of the back-to-back converter is simplified as a 1200 V DC voltage source. Each wind farm consists of 22 turbines, each with a capacity of 3.15 MW. This section mainly verifies the effectiveness of the control strategy under start-up and steady-state operation of wind farms, power fluctuation and low-voltage faults in the offshore AC system.

To simplify the analysis, we model all the WTs in a wind farm as a single large-capacity WT.

**Table 1.** Parameters of the Offshore AC System via DRU-HVDC.

| Parameter Category | Parameter Name | Value |
|---|---|---|
| Onshore AC System | Rated Capacity | 200 MW |
| | Rated AC Voltage | 66 kV |
| | Resistance | 0.396 Ω |
| | Inductance | 0.0126 H |
| Onshore converter | Filter Resistance | 0.396 Ω |
| | Filter Inductance | 0.0126 H |
| DC Transmission | DC Support Capacitance | 0.001 F |
| | Flat Reactor Inductance | 0.26 H |
| | Resistance | 0.011 Ω/km |
| | Inductance | 0.0026 H/km |
| | Capacitance | 0.2185 μF/km |
| | Length of DC cable | 500 km |
| Diode Rectifier | Transformer Ratio | 66 kV/50 kV |
| Second-order High-pass Filter | $C_{a1}$ | 28.865 μF |
| | $L_a$ | 31.589 mH |
| | $R_{a1}$ | 6.891 Ω |
| | $C_{a2}$ | 320.69 μF |
| | $R_{a2}$ | 60.639 Ω |

**Table 1.** *Cont.*

| Parameter Category | Parameter Name | Value |
|---|---|---|
| C-type Filter | $C_b$ | 28.865 μF |
| | $L_b$ | 3.149 mH |
| | $R_b$ | 19.291 Ω |
| Reactive Compensation Capacitor | $C_f$ | 4.7924 μF |
| AC Line | Resistance | 0.00843 Ω/km |
| | Inductance | 2.5 μH/km |
| | Transformer T2 Ratio | 35 kV/66 kV |
| | Length of AC cable | 100 km |
| Wind Turbine | Capacity | 3.15 MW |
| | Number of Turbines | 22 |
| | Transformer Ratio | 0.69 kV/35 kV |
| | DC Voltage | 1.2 kV |
| Control parameters of GSC | Active Power Controller | K: 0.01; J: 16 |
| | Reactive power controller | n: $3.577 \times 10^{-5}$ |

### *3.1. Simulation Case: Start-Up and Pre-Synchronization of DRU-HVDC*

In the analyzed case, wind turbines are started up sequentially, as illustrated in Figure 8. The detailed start-up procedure in this simulation case is as follows:

Initially, the first WT is started, and the GSC of the first WT is unlocked, operating under CF control at this stage. Meanwhile, the breaker closes, connecting the first GSC to the offshore DRU system and precharging the capacitor of the HVDC bus. The GSC operates unloaded, increasing the output voltage linearly from zero to 1 p.u. with a frequency reference value of 50 Hz. From t = 1 s to t = 3 s, the GSC of the WT operates under CVCF control. At t = 3 s, the GSC transitions from CVCF to GFM control. With the power controller, the active power reference value increases linearly from zero to 1 p.u. to establish the offshore AC grid. The startup procedure for the rest WTs is similar to that of the first WT, with a key difference: the breakers close only after the startup procedure is complete. And pre-synchronization is employed before connection. In this case, the second WT connects to the offshore AC grid at t = 6 s, followed by the third WT at t = 10 s.

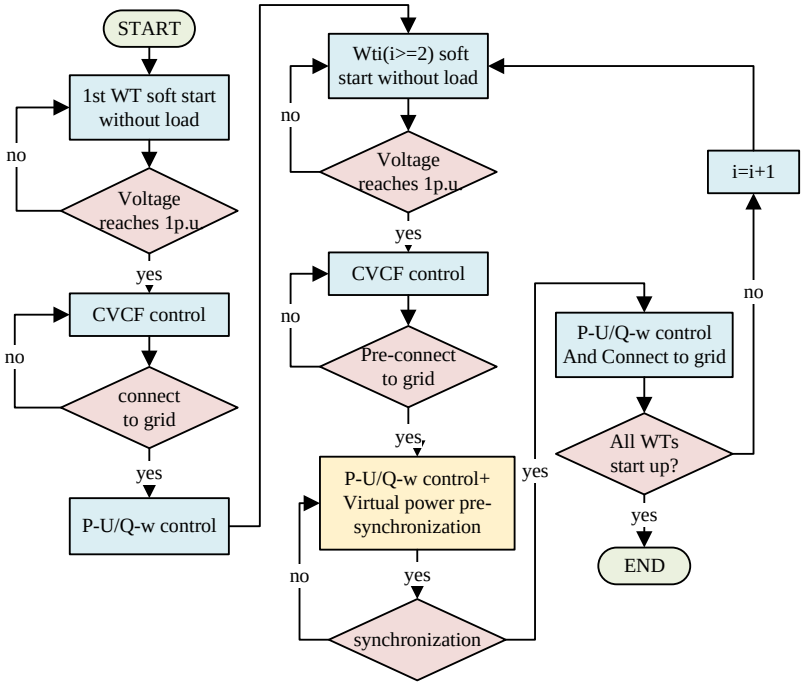


**Figure 8.** Start-up procession of wind farms.

The start-up and steady-state operation results are presented in Figure 9. The results indicate that the voltage of the offshore AC grid is 1.053 p.u., and the frequency is 49.996 Hz. The output active power of GSC of WT is 182.38 MW, while the reactive power is 1.19 MVar, exhibiting a high power factor and low THD in steady-state operation. New WTs integrate into the offshore grid smoothly in Figure 9.

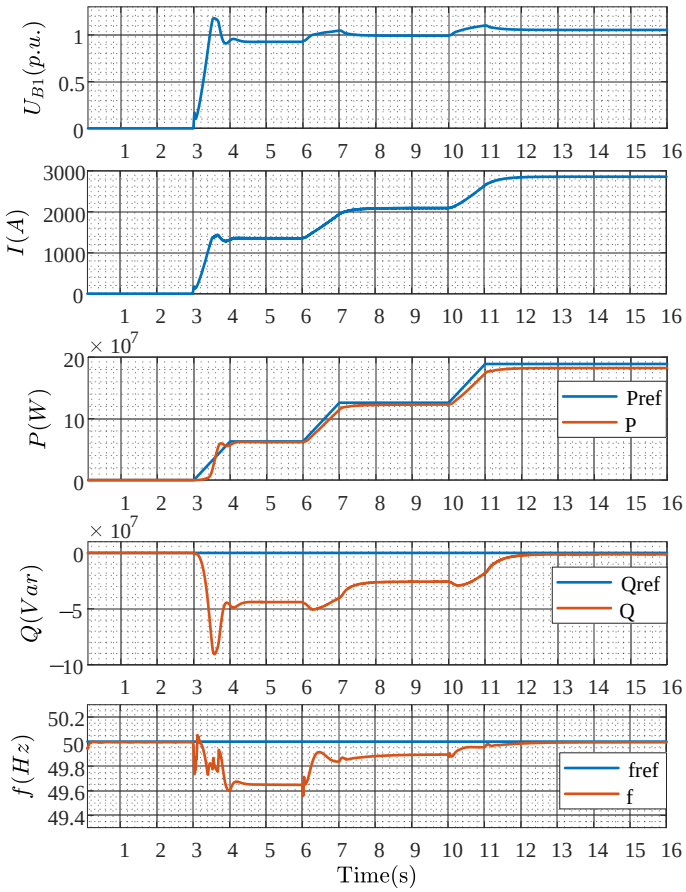


**Figure 9.** Results of Steady-State Operation of Multiple WTs.

After applying the proposed control, the system output power changes smoothly. The overshoot of voltage and current is minimal when new WTs are connected. In the steady state, the three WTs share power according to their capacity. The system exhibits the characteristics of a strong droop in the Q-$\omega$ controller and operates near the full power factor after all WTs are connected. Frequency fluctuation of the offshore AC grid remains minimal under both transient and steady-state operating conditions.

In the simulation case, the impact of pre-synchronization is assessed. The effect of pre-synchronization on voltage fluctuations is compared by implementing and removing the pre-synchronization method, as shown in Figure 10. It is clear that with virtual power pre-synchronization, voltage overshoot is effectively reduced compared to the scenario without synchronization. The phase obtained in advance by the virtual power method leads to minimal frequency fluctuations in the offshore grid. By employing virtual power pre-synchronization, the overall stability of the transmission system is significantly improved.

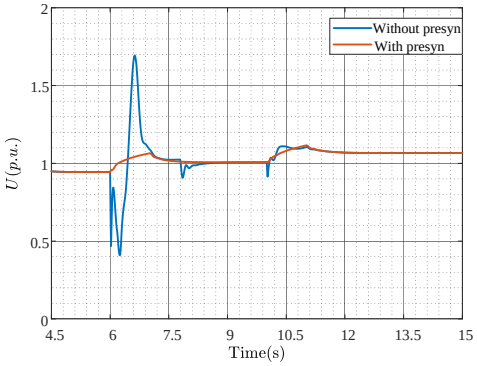


**Figure 10.** Comparison of pre-synchronization results.

### *3.2. Simulation Case: Power Disturbances*

Based on the proposed start-up strategy, all WTs have been started and are in normal operation. To verify the effectiveness of the proposed GFM control under power disturbances, a simulation considering power fluctuation is conducted. The power disturbance conditions are as follows: at t = 13 s, the reference power of the second WT is suddenly reduced to 0.5 p.u.; at t = 17 s, the reference power of the third WT is suddenly reduced to 0.7 p.u.; at t = 21 s, the reference power of the second WT suddenly increases to 0.8 p.u.; at t = 25 s, the reference power of the third WT suddenly increases to 1.2 p.u.

According to Figure 11, during the entire power fluctuation process, the system voltage is maintained between 0.9 p.u. and 1.16 p.u., while the frequency is controlled within the range of 49.7 Hz to 50.23 Hz. These results show that the proposed method ensures synchronous and stable operation of WTs under sudden power changes. Consequently, the system demonstrates strong robustness and stability in the presence of abrupt power variations.

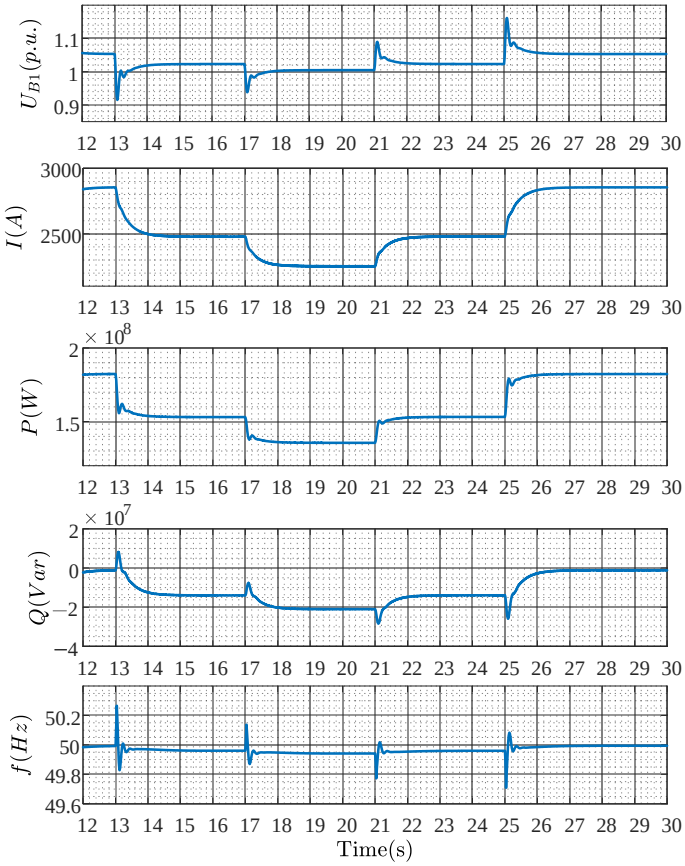


**Figure 11.** Results of power disturbances.

### *3.3. Simulation Case: Offshore Low Voltage Ride-Through*

A low-voltage fault is applied at point B1 to simulate offshore low-voltage ride-through and verify the effectiveness of the improved control. The simulated fault consists of a 60% voltage drop, which begins at 8 s and lasts for 1.5 s.

Figure 12 illustrates the low-voltage fault condition in the offshore AC grid. Three control strategies, CL, FVI, along with AVI, are evaluated in the simulation. As for the current limiting method, the fault current reaches 1.29 p.u. after fault, with a recovery time of 3.5 s. By implementing the FVI method, the maximum current is 1.185 p.u., while the recovery time shortens to 0.7 s. The proposed adaptive virtual impedance method achieves 1.11 p.u. peak current, and recovers within 0.6 s. The simulation also shows the proposed AVI method exhibits the lowest voltage overshoot with 0.03 p.u., while FVI with 0.05 p.u. and CL with 0.11 p.u. Similarly, the recovery speed of frequency, as well as active and reactive power, is faster with the AVI method compared to the CL and FVI methods. The proposed AVI method effectively protects the transmission system during faults, with no overshoot observed during the recovery process, and returns to normal after the fault is cleared. The AVI method exhibits smaller voltage and current overshoots during faults compared to the traditional CL and FVI methods and achieves faster recovery. Additionally, the AVI method suppresses fault currents and enables rapid system recovery effectively.

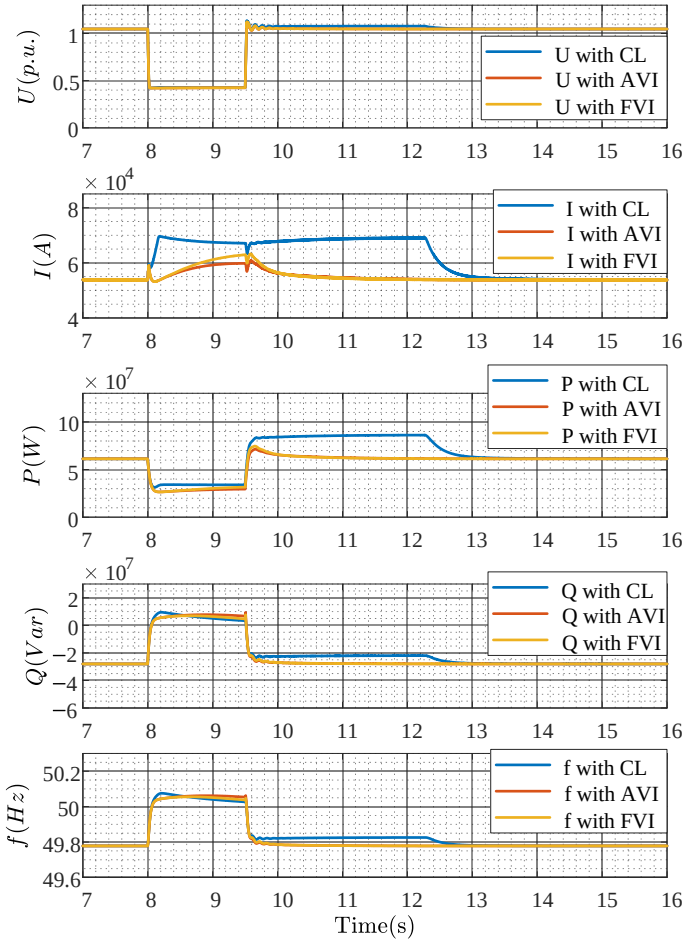


**Figure 12.** Comparison of low-voltage fault results in offshore AC grid with current limiting(CL), fixed virtual impedance(FVI) and adaptive virtual impedance(AVI).

## 4. Discussion

In this section, a comprehensive comparison and discussion of the proposed method and existing methods is presented.

### *4.1. Discussion on Control Strategy*

The previous research findings indicate that in offshore wind farm systems, the lack of rotational inertia results in a negligible coupling relationship between the active power emitted by the inverter and the system frequency [12]. To achieve higher inertia and self-synchronization at one time, an advanced GFM control with reactive power self-synchronization is proposed. While the characteristics of the uncontrollable transmission system are distinct from those of the controllable transmission system. The power droop feature is caused by the characteristics of diodes, which are fundamentally different from the power relationship caused by resistive line characteristics. Thus, the P-U and Q-$\omega$ droop control strategies are introduced into the control loop, fulfilling the output feature of the DRU-HVDC system. Additionally, the self-synchronization method exhibits high immunity during power disturbance, offering high reliability for the transmission system. Compared to the distributed PLL-based control strategy [9], the proposed control strategy demonstrates superior performance in weak grid conditions and is capable of achieving self-synchronization. The self-synchronization mechanism and the proposed droop control are validated by the power disturbance results in Figure 11, which demonstrate the robustness of the proposed control strategy. The proposed method fulfills the requisite robustness, reliable performance and plug-and-play criteria for the GFM-based DRU-HVDC system.

### *4.2. Discussion on Start-Up Performance*

In order to consolidate the contribution of the proposed pre-synchronization, the start-up strategy is compared by the power synchronization method with virtual power pre-synchronization and with power synchronization only.

The initial phase is determined by the virtual power and the relevant phase calculation is collected without the use of a PLL through the adoption of virtual power-based pre-synchronization. Figure 10 illustrates that the integration of a new WT into an offshore AC grid results in an abrupt voltage spike, with a surge reaching 0.4 p.u. The voltage spike without pre-synchronization is significantly larger than that observed in the proposed virtual power-based pre-synchronization method, which exhibited a surge of 0.05 p.u. The simulation results also demonstrate that the GSCs can integrate into the grid in a seamless manner with the proposed virtual power-based pre-synchronization method.

PLL is a widely used pre-synchronization technique. However, it can introduce instability under weak grid conditions. The proposed pre-synchronization method can accurately control the frequency/phase of GSC output voltage and maintain system stability when GSCs are connected to the grid. The phase can be obtained without the necessity of PLL. During the pre-synchronization process, the virtual power synchronization method can prevent excessive impact on the power grid and allow for a seamless connection. In contrast to the conventional PLL-based pre-synchronization method [9], this method can be employed within GFM control directly. The PLL method needs a mode transition between pre-synchronization and GFM control. The smooth transition of virtual power-based pre-synchronization illustrates significant stability and transient performance improvements in the proposed strategy for new WT integration.

### *4.3. Discussion on Different LVRT Control Strategies*

For GFM-based converters, reduced current during LVRT leads to lower investment in power electronic components and enhances the reliability of the power transmission system. To demonstrate the effectiveness of the proposed method in mitigating fault current, the system employing the LVRT technique is compared with conventional methods presented in [26,28], as shown in Figure 12.

For current-limiting control, GSCs operate similarly as a constant current source when a fault occurs. Their FRT strategy is grounded in the principle of current saturation, a concept frequently employed in cascaded voltage and current loops. This mechanism operates by integrating fault current, which causes the current loop to saturate and subsequently reduces the output duty cycle. This control scheme is particularly suitable for scenarios

where transient performance is not a primary concern. When GSCs are connected to DRU, the desaturation time for the current loop is notably prolonged, and the mode transition becomes complex. The simulation results in Figure 12 illustrate the phenomenon. The current reaches a peak value of 1.29 p.u. after a fault occurs at 0.2 s, gradually saturating to 1.25 p.u. over 1.4 s. Once the fault is cleared, the current initially rises to 1.3 p.u., with the restoration process lasting for 4 s. The overshoot behavior is also observed in both active and reactive power. The duration of the transient over-current condition is prolonged due to current saturation and limited control bandwidth, which is unfavorable for GFM control and the over-current stability of DRU. Therefore, the CL-based LVRT strategy is not suitable for this scenario.

In FVI-based LVRT control, voltage compensation is linearly dependent on current. A voltage droop is applied to the voltage reference when the fault happens, and current limitation is also adopted. Nevertheless, this approach necessitates impedance adjustments to limit current under different low-voltage conditions. The results presented in Figure 12 indicate that the current reached a peak value of 1.17 p.u. following the fault event. Concerning the FVI proposed in [28], current damping has been enhanced compared to the CL discussed in [26]. The system returns to its equilibrium point stably within 2 s. The active and reactive power changes are lower than CL during the whole LVRT procession. By employing the virtual impedance method, the output voltage is directly reduced through the virtual droop of the reference, resulting in improved performance compared to the CL-based LVRT strategy. However, the reference droop varies linearly with the fault current, leading to a slow suppression of the fault current. FVI demonstrates superior performance compared to CL, further enhancements are still required.

In the proposed AVI-based LVRT strategy, the voltage droop is adaptively adjusted in relation to the current. The droop impedance increases quadratically with fault current. This approach results in enhanced voltage droop capability during fault conditions. As for the simulation results depicted in Figure 12, the current reaches a peak value of 1.11 p.u. after the fault, representing the lowest peak among all methods evaluated. When the fault is cleared, the current overshoot is 0.12 p.u., which is less than that observed in the aforementioned methods. Furthermore, active power remains consistently lower than that of the other approaches throughout the entire process. By considering the X/R ratio, the proposed AVI control strategy demonstrates superior fault performance compared to the CF and FVI-based LVRT strategies. The proposed approach exhibits the lowest overshoot and the fastest recovery capability, making it suitable for LVRT. By adjusting impedance based on fault current, the AVI method effectively suppresses fault current without requiring additional modifications. Therefore, the proposed AVI-based LVRT method meets the requirements for a reliable power transmission system and shows better LVRT performance than previous studies.

## 5. Conclusions

This paper proposes an enhanced grid-forming control strategy for offshore wind turbines connected to the DRU-HVDC system. The strategy includes reactive power self-synchronization, virtual power-based pre-synchronization, and an adaptive virtual impedance controller. Simulation results show that the proposed pre-synchronization method effectively mitigates the adverse effects of inconsistencies in voltage amplitude and phase difference. Additionally, the adaptive virtual impedance control addresses overcurrent issues during LVRT in the offshore AC system, enabling rapid fault recovery. Thus, the proposed GFM control method effectively meets the startup, synchronization, and LVRT requirements of offshore wind turbines, making it particularly suitable for offshore wind farms connected via DRU-HVDC. Notably, compared to existing studies, the proposed pre-synchronization and adaptive virtual impedance strategy demonstrate smoother transitions and enhanced recovery performance during both the startup process and fault conditions.

**Author Contributions:** Conceptualization, Y.Z. and H.W.; methodology, Y.Z., H.W. and N.L.; validation, Y.Z.; formal analysis, Y.Z., N.L. and S.L.; investigation, Y.Z. and S.L.; writing and original draft preparation, Y.Z.; writing, review and editing, Y.Z., N.L. and S.L.; visualization, Y.Z., W.Z. and C.T.; supervision, H.W.; project administration, H.W.; funding acquisition, H.W. All authors have read and agreed to the published version of the manuscript.

**Funding:** This work was supported in part by the GuangDong Basic and Applied Basic Research Foundation (Offshore Wind Power Joint Fund) under grant 2022A1515240030 and China General Nuclear Power Group(grant number 008-ZB-B-2022-C30-01231).

**Data Availability Statement:** The original contributions presented in the study are included in the article, further inquiries can be directed to the corresponding author.

**Conflicts of Interest:** Authors Wenjiang Zhu and Checng Tang were employed by the company China Nuclear Power Technology Research Institute Co., Ltd. The remaining authors declare that the research was conducted in the absence of any commercial or financial relationships that could be construed as a potential conflict of interest.

## References

1. Herrmann, M.; Alkemper, M.; Hofmann, L. Analysis of Onshore Synthetic Inertia and Primary Control Reserve Contributions of Alternating Current-Side Meshed Offshore Grids with Voltage-Source Converter and Diode Rectifier Unit High-Voltage Direct Current Connections. *Energies* **2023**, *16*, 6700. [CrossRef]
2. Jin, Y.; Zhang, Z.; Huang, Y.; Xu, Z.; Xu, F. Harmonic filtering and fault ride-through of diode rectifier unit and modular multilevel converter based offshore wind power integration. *IET Renew. Power Gener.* **2023**, *17*, 3554–3567. [CrossRef]
3. Erlich, I.; Shewarega, F.; Feltes, C.; Koch, F.W.; Fortmann, J. Offshore Wind Power Generation Technologies. *Proc. IEEE* **2013**, *101*, 891–905. [CrossRef]
4. Oni, O.E.; Davidson, I.E.; Mbangula, K.N. A review of LCC-HVDC and VSC-HVDC technologies and applications. In Proceedings of the 2016 IEEE 16th International Conference on Environment and Electrical Engineering (EEEIC), Florence, Italy, 7–10 June 2016; pp. 1–7.
5. Saborio-Romano, O.; Bidadfar, A.; Goksu, O.; Zeni, L.; Cutululis, N.A. Power Oscillation Damping from Offshore Wind Farms Connected to HVDC via Diode Rectifiers. *Energies* **2019**, *12*, 3387. [CrossRef]
6. Herrera, D.; Galván, E.; Carrasco, J.M. Method for controlling voltage and frequency of the local offshore grid responsible for connecting large offshore commercial wind turbines with the rectifier diode-based HVDC-link applied to an external controller. *IET Electr. Power Appl.* **2017**, *11*, 1509–1516. [CrossRef]
7. Blasco-Gimenez, R.; Ano-Villalba, S.; Rodríguez-D'Derlée, J.; Morant, F.; Bernal-Perez, S. Distributed voltage and frequency control of offshore wind farms connected with a diode-based HVdc link. *IEEE Trans. Power Electron.* **2010**, *25*, 3095–3105. [CrossRef]
8. Prignitz, C.; Eckel, H.G.; Rafoth, A. FixReF sinusoidal control in line side converters for offshore wind power generation. In Proceedings of the 2015 IEEE 6th International Symposium on Power Electronics for Distributed Generation Systems (PEDG), Aachen, Germany, 22–25 June 2015; IEEE: Piscataway, NJ, USA, 2015; pp. 1–5.
9. Yu, L.; Li, R.; Xu, L. Distributed PLL-based control of offshore wind turbines connected with diode-rectifier-based HVDC systems. *IEEE Trans. Power Deliv.* **2017**, *33*, 1328–1336. [CrossRef]
10. Xiao, H.; Huang, X.; Huang, Y.; Liu, Y. Self-synchronizing control and frequency response of offshore wind farms connected to diode rectifier based HVDC system. *IEEE Trans. Sustain. Energy* **2022**, *13*, 1681–1692. [CrossRef]
11. Iván, A.A.; Ruben, P.G.; Blasco-Gimenez, R.; Javier, R.A. Control strategy of a HVDC-Diode Rectifier connected type-4 off-shore wind farm. In Proceedings of the 2015 IEEE 2nd International Future Energy Electronics Conference (IFEEC), Taipei, Taiwan, 1–4 November 2015; IEEE: Piscataway, NJ, USA, 2015; pp. 1–6.
12. Huang, X.; Xiao, H.; Huang, Y.; Liu, T.; Yang, P. Black Start Strategy of DRU-Based Low-Frequency AC Transmission System for Offshore Wind Power Integration. In Proceedings of the 2023 IEEE Industry Applications Society Annual Meeting (IAS), Nashville, TN, USA, 29 October–2 November 2023; pp. 1–8.
13. Chang, Y.; Cai, X. Hybrid Topology of a Diode-Rectifier-Based HVDC System for Offshore Wind Farms. *IEEE J. Emerg. Sel. Top. Power Electron.* **2019**, *7*, 2116–2128. [CrossRef]
14. Saborío-Romano, O.; Bidadfar, A.; Sakamuri, J.N.; GÃűksu, ÃŰ.; Cutululis, N.A. Novel Energisation Method for Offshore Wind Farms Connected to HVdc via Diode Rectifiers. In Proceedings of the IECON 2019—45th Annual Conference of the IEEE Industrial Electronics Society, Lisbon, Portugal, 14–17 October 2019; Volume 1, pp. 4837–4841.
15. Xie, L.; Yao, L.; Cheng, F.; Li, Y.; Liang, S. Coordinate control strategy for stability operation of offshore wind farm integrated with Diode-rectifier HVDC. *Glob. Energy Interconnect.* **2020**, *3*, 205–216. [CrossRef]
16. Zhang, L.; Harnefors, L.; Nee, H.P. Power-Synchronization Control of Grid-Connected Voltage-Source Converters. *IEEE Trans. Power Syst.* **2010**, *25*, 809–820. [CrossRef]

17. Lu, M. An Inrush Current Limiting Strategy for Virtual-Oscillator-Controlled Grid-Forming Inverters. *IEEE Trans. Energy Convers.* **2023**, *38*, 1501–1510. [CrossRef]
18. Opila, D.F.; Kintzley, K.; Shabshab, S.; Phillips, S. Virtual Oscillator Control of Equivalent Voltage-Sourced and Current-Controlled Power Converters. *Energies* **2019**, *12*, 298. [CrossRef]
19. Kuang, Yulin; Ma, Fujun and Yang, Cheng and Peng, Qiaoling and Huang, Gelin. Pre-Synchronization Control Strategy for Virtual Synchronous Generator Grid Connection Based on Voltage Mathematical Relationships. *IEEE Access.* **2024**, *12*, 35854–135863. [CrossRef]
20. Li, R.; Yu, L.; Xu, L. Offshore AC Fault Protection of Diode Rectifier Unit-Based HVdc System for Wind Energy Transmission. *IEEE Trans. Ind. Electron.* **2019**, *66*, 5289–5299. [CrossRef]
21. Ghany, A.A.; Shehata, E.G.; Elsayed, A.H.M.; Mohamed, Y.S.; Haes Alhelou, H.; Siano, P.; Diab, A.A.Z. Novel Switching Frequency FCS-MPC of PMSG for Grid-Connected Wind Energy Conversion System with Coordinated Low Voltage Ride Through. *Electronics* **2021**, *10*, 492. [CrossRef]
22. Feyzi, M.; Roozbehani, S.; Liasi, S.G. Low Voltage Ride Through Improvement of Machine Side and Grid Side Converters of PMSG-Wind Turbine Based on SMC. In Proceedings of the 2022 13th Power Electronics, Drive Systems, and Technologies Conference (PEDSTC), Tehran, Iran, 1–3 February 2022; pp. 251–257.
23. Kim, C.; Kim, W. Low-Voltage Ride-Through Coordinated Control for PMSG Wind Turbines Using De-Loaded Operation. *IEEE Access* **2021**, *9*, 66599–66606. [CrossRef]
24. Chen, T.; Chen, L.; Zheng, T.; Mei, S. LVRT Control Method of Virtual Synchronous Generator Based on Mode Smooth Switching. *Power Syst. Technol.* **2016**, *40*, 2134–2140. (In Chinese)
25. Vasquez, J.C.; Guerrero, J.M.; Savaghebi, M.; Eloy-Garcia, J.; Teodorescu, R. Modeling, analysis, and design of stationary-reference-frame droop-controlled parallel three-phase voltage source inverters. *IEEE Trans. Ind. Electron.* **2012**, *60*, 1271–1280. [CrossRef]
26. Liu, J.; Miura, Y.; Ise, T. Comparison of dynamic characteristics between virtual synchronous generator and droop control in inverter-based distributed generators. *IEEE Trans. Power Electron.* **2015**, *31*, 3600–3611. [CrossRef]
27. Lu, F.; He, A.; Hou, K.; Wang, X. Low-voltage ride-through control strategy of virtual synchronous generator based on all-pass filter. *Electr. Power Autom. Equip.* **2019**, *39*, 176–181.
28. Wang, Y.; Sun, D.; Wang, X.; Zhang, L. A novel low voltage ride through control strategy based on virtual synchronous generator. In Proceedings of the 2019 IEEE 28th International Symposium on Industrial Electronics (ISIE), Vancouver, BC, Canada, 12–14 June 2019; IEEE: Piscataway, NJ, USA, 2019; pp. 2105–2110.
29. Yu, L.; Miao, S.; Zhu, J.; Fu, Z.; Li, R.; Zhao, C. Self-synchronization control of offshore wind turbines connected with DRU-HVDC. *CSEE J. Power Energy Syst.* **2023**, 1–11.
30. Zhang, Z.; Jin, Y.; Xu, Z. Grid-forming control of wind turbines for diode rectifier unit based offshore wind farm integration. *IEEE Trans. Power Deliv.* **2022**, *38*, 1341–1352. [CrossRef]
31. Paquette, A.D.; Divan, D.M. Virtual impedance current limiting for inverters in microgrids with synchronous generators. *IEEE Trans. Ind. Appl.* **2014**, *51*, 1630–1638. [CrossRef]
32. Qoria, T.; Wu, H.; Wang, X.; Colak, I. Variable Virtual Impedance-Based Overcurrent Protection for Grid-Forming Inverters: Small-Signal, Large-Signal Analysis and Improvement. *IEEE Trans. Smart Grid* **2023**, *14*, 3324–3336. [CrossRef]


**Disclaimer/Publisher's Note:** The statements, opinions and data contained in all publications are solely those of the individual author(s) and contributor(s) and not of MDPI and/or the editor(s). MDPI and/or the editor(s) disclaim responsibility for any injury to people or property resulting from any ideas, methods, instructions or products referred to in the content.